P122 | Advanced Topics in Plasma Physics

Magnetogenesis and Small-Scale Dynamo

Instructor: Muni Zhou

This chapter examines how magnetic fields are generated and how turbulent motions amplify them to dynamically significant strengths. We begin with observations in galaxies, galaxy clusters, and intergalactic voids, emphasizing constraints on both field strength and spatial scale. After an overview of possible primordial and astrophysical origins, we develop two seed-field mechanisms: the Biermann battery, driven by misaligned gradients of electron density and temperature, and the Weibel instability, driven by temperature anisotropy or counter-streaming flows. Laboratory experiments and kinetic simulations illustrate these mechanisms and their interplay.

We then follow the amplification of a weak seed by the small-scale turbulent dynamo. Flux freezing explains how stretching strengthens a field, while magnetic diffusion and anti-dynamo theorems establish the importance of conductivity and flow geometry. We identify the eddies responsible for kinematic growth, compare the viscous and resistive scales at high and low magnetic Prandtl number, and relate folded magnetic structures to their spectra. Magnetic back reaction then leads to nonlinear growth and eventual saturation. Physical arguments, scaling estimates, and schematics connect these stages through the source of magnetic energy, the competing timescales, and the evolving field geometry.

Dartmouth College

Graduate plasma physics

Contents

1 Observations: magnetic strength and magnetic scale **1**
1.1 What must a theory explain? . . . 1
1.2 Galaxies and clusters: synchrotron emission and Faraday rotation . . . 1
1.3 Intergalactic Magnetic Fields and Voids . . . 2

2 Possible origins and subsequent amplification **3**
2.1 Primordial fields . . . 3
2.2 Astrophysical injection and in-situ production . . . 3
2.3 Notation and physical regimes . . . 4

3 The Biermann battery **4**
3.1 From the electron force balance to a magnetic source . . . 4
3.2 Geometry, direction, and the vorticity analogy . . . 5
3.3 How much field is produced? . . . 5
3.4 When does induction compete with the battery? . . . 6
3.5 Laser-produced fields and their reconnection . . . 6

4 Weibel Instability **7**
4.1 Thermal Weibel Instability . . . 7
4.2 Counter-streaming Beams . . . 9

5 From a seed field to dynamo amplification **10**
5.1 The question changes: can the field keep growing? . . . 10
5.2 Stretching a flux tube: where the energy comes from . . . 10
5.3 Why a single stretch is not yet a dynamo . . . 11
5.4 The planar anti-dynamo theorem . . . 11
5.5 Cowling's theorem: axisymmetry cannot sustain the field . . . 12

6 Kinematic turbulent dynamo: rates, folds, and spectra **13**
6.1 Which eddies stretch the field fastest? . . . 13
6.2 What does the amplified field look like? . . . 14
6.3 High magnetic Prandtl number: two different cutoffs . . . 15
6.4 Brief contrast: low magnetic Prandtl number . . . 16
6.5 High magnetic Prandtl number: the kinematic spectrum . . . 17

7 Back reaction, nonlinear growth, and saturation **18**
7.1 Which motions feel the field first? . . . 18
7.2 Nonlinear growth and approach to equipartition . . . 18
7.3 Connections to reconnection and plasma physics . . . 19

Recommended reading **20**

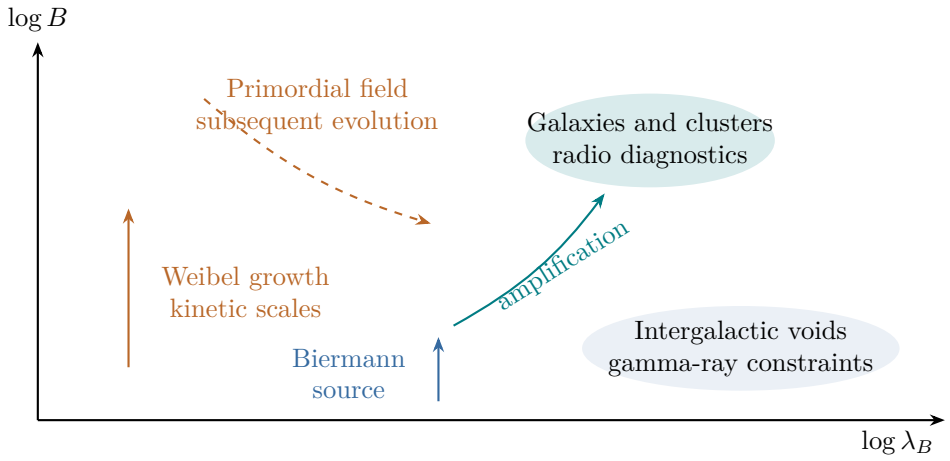
References **20**

1 Observations: magnetic strength and magnetic scale

1.1 What must a theory explain?

Magnetic reconnection and MHD turbulence describe the evolution of an existing magnetic field. Magnetogenesis asks an earlier question: how did that field first appear? A successful account must also explain how a weak seed becomes dynamically significant and how its correlation length evolves.

We will distinguish the field strength $B_{\rm rms} = \langle B^2 \rangle^{1/2}$ from a magnetic correlation length λ_B, over which the field direction remains correlated. Two fields with the same energy can affect particles very differently if their correlation lengths differ. Figure 1 organizes the opening questions in this two-dimensional space.



Conceptual map only: regions and arrows are not numerical observational bounds or universal evolutionary tracks. Comparisons require a specified epoch and a consistent definition of scale.

Figure 1: Field strength and coherence are separate parts of the magnetogenesis problem. Cosmic environments motivate the questions; different production and amplification mechanisms operate on different scales.

1.2 Galaxies and clusters: synchrotron emission and Faraday rotation

Relativistic electrons spiralling in a magnetic field emit synchrotron radiation. Its intensity depends on both the magnetic field and the relativistic-electron population; linear polarization carries information about the projected field orientation and order. Radio emission therefore supplies evidence for magnetization, but intensity alone is not a unique measurement of B.

Faraday rotation probes a different combination of quantities. A linearly polarized wave propagating through magnetized plasma has its polarization angle rotated by

$$\Delta\chi = \mathrm{RM}\,\lambda_{\rm rad}^2, \qquad \mathrm{RM} = 0.812 \int \frac{n_e}{\mathrm{cm^{-3}}} \frac{B_{\rm los}}{\mu\mathrm{G}} \frac{\mathrm{d}l}{\mathrm{pc}} \quad \mathrm{rad\,m^{-2}}. \tag{1.1}$$

Here $\lambda_{\rm rad}$ is the observing wavelength, not λ_B. The displayed coefficient is for a nearby source; a cosmological contribution includes the appropriate redshift factor. Reversals can cancel in the line integral, so inferring a field strength also requires information about electron density and magnetic structure. These complementary measurements support microgauss-level fields in many galaxies and galaxy clusters [1, 2].

The intracluster medium (ICM) provides a useful scale comparison. Representative conditions are $n_e \sim 10^{-4}$–$10^{-2}\,\mathrm{cm^{-3}}$ and $T \sim 10^7$–$10^8\,\mathrm{K}$, with substantial variation between cluster cores and outskirts. Even when the thermal pressure exceeds the magnetic pressure, the field can compete with subsonic

turbulent motions. For a hydrogen plasma,

$$v_A = \frac{B}{\sqrt{4\pi\rho}} \simeq 154\,\mathrm{km\,s^{-1}} \left(\frac{B}{10\,\mu\mathrm{G}}\right) \left(\frac{n_i}{0.02\,\mathrm{cm^{-3}}}\right)^{-1/2}. \tag{1.2}$$

Hitomi measured a line-of-sight velocity dispersion of $164 \pm 10\,\mathrm{km\,s^{-1}}$ in the Perseus core at projected radii of approximately 30–60 kpc [3]. This is a measured one-dimensional dispersion, not a direct measurement of a driving scale or of three-dimensional kinetic–magnetic equipartition. Nevertheless, the comparison shows why a field that is weak relative to thermal pressure may matter dynamically.

1.3 Intergalactic Magnetic Fields and Voids

Far from luminous objects, radio measurements become difficult. High-energy gamma rays offer another route. A TeV photon from a blazar or gamma-ray burst can pair-produce on the extragalactic background light (EBL), injecting an electron and positron. Those particles upscatter cosmic microwave background (CMB) photons by inverse Compton scattering, producing secondary gamma rays, often in the GeV band. An intervening magnetic field deflects the charged particles and can broaden or delay the secondary signal [4, 5].

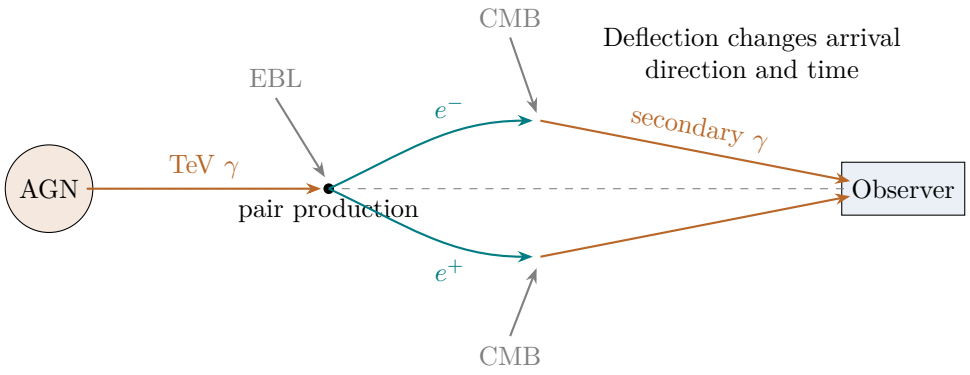


Figure 2: The pair-cascade geometry. The primary gamma ray is neutral; the intermediate electron and positron are deflected. The drawing exaggerates the angles. A missing or delayed cascade constrains a model of the source, propagation, and field.

For an ultrarelativistic particle with energy E_e, the Larmor radius in Gaussian units is

$$r_L = \frac{p_e c}{eB} \simeq \frac{E_e}{eB} \simeq 108\,\mathrm{Mpc} \left(\frac{E_e}{1\,\mathrm{TeV}}\right) \left(\frac{B}{10^{-17}\,\mathrm{G}}\right)^{-1}. \tag{1.3}$$

Let ℓ_{IC} be its inverse-Compton cooling length. In the small-angle limit,

$$\theta \sim \begin{cases} \ell_{\mathrm{IC}}/r_L, & \lambda_B \gtrsim \ell_{\mathrm{IC}}, \\ \sqrt{\ell_{\mathrm{IC}}\lambda_B}/r_L, & \lambda_B \ll \ell_{\mathrm{IC}}. \end{cases} \tag{1.4}$$

In the first case the force has approximately one direction during cooling. In the second, the particle crosses $N \sim \ell_{\mathrm{IC}}/\lambda_B$ uncorrelated cells: each contributes λ_B/r_L, and the changes add as $\sqrt{N}$. Thus a fixed deflection constrains $B\lambda_B^{1/2}$ at short correlation length and gives a bound scaling as $B_{\min} \propto \lambda_B^{-1/2}$.

The non-detection of a predicted cascade does not give a universal magnetic-field threshold. The inference depends on the intrinsic source spectrum and history, the observing window, background radiation, and competing pair-energy-loss processes. For example, one analysis of GRB 221009A obtained a lower bound of order 10^{-19} G for correlation lengths above 1 Mpc, with stronger bounds at shorter scales [5]. Different blazar analyses give different numerical bounds. The robust lesson for this lecture is the joint dependence on *strength and correlation length.*

Three questions organize the rest of the notes: What creates a seed? What amplifies its energy? What determines its correlation scale and spatial filling? Observations constrain different combinations of these properties.

2 Possible origins and subsequent amplification

2.1 Primordial fields

Primordial scenarios place magnetic-field generation before galaxies and clusters form. Proposed settings include inflation and cosmological phase transitions, such as the electroweak or QCD transitions. Inflationary magnetogenesis requires additional physics beyond conformally invariant Maxwell theory in an expanding vacuum. Causal post-inflationary processes initially correlate fields over scales limited by their causal horizon. These are possible origins, not established identifications of the observed field [1].

Cosmic expansion and plasma evolution then alter both strength and scale. For ideal expansion without additional turbulent processing,

$$B_{\mathrm{physical}} \propto a^{-2}, \qquad \lambda_{\mathrm{physical}} \propto a, \tag{2.1}$$

where a is the cosmological scale factor. It is therefore useful to compare $a^2 B_{\mathrm{physical}}$ and $\lambda_{\mathrm{physical}}/a$. Turbulent decay and helicity constraints can further change these comoving quantities. Recombination, reionization, and structure formation change the relevant plasma environment. The aim here is to recognize these stages, rather than derive a particular cosmological model.

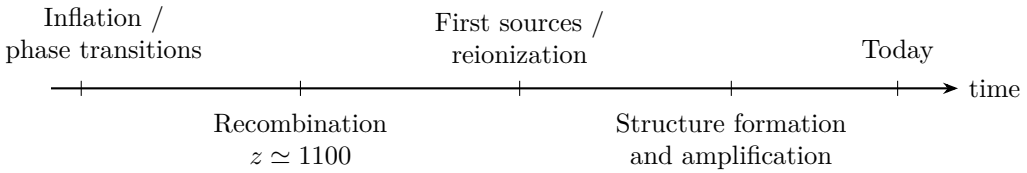


Figure 3: A schematic sequence of environments relevant to magnetic-field evolution. The time axis is not to scale, and structure formation overlaps several stages.

2.2 Astrophysical injection and in-situ production

Galaxies, stellar outflows, and AGN jets can inject magnetized material into their surroundings. This offers an "inside-out" route to magnetizing larger volumes. It must explain both where the injected field was generated and how far it spreads. In-situ processes instead generate a field within the plasma being considered, through pressure gradients or an unstable particle distribution. These routes can operate together [2].

A dynamo then transfers mechanical energy into magnetic energy. It is an amplification mechanism and does not, in the usual MHD description, solve the strictly zero-field initial-value problem. With constant magnetic diffusivity η,

$$\frac{\partial \boldsymbol{B}}{\partial t} = \boldsymbol{\nabla} \times (\boldsymbol{U} \times \boldsymbol{B}) + \eta \nabla^2 \boldsymbol{B} \tag{2.2}$$

is homogeneous in $\boldsymbol{B}$: if $\boldsymbol{B}$ is identically zero initially, it remains zero. A battery supplies an additional source. A kinetic instability amplifies microscopic electromagnetic fluctuations about an unmagnetized equilibrium. "Initially unmagnetized" means no dynamically relevant macroscopic field; it does not exclude fluctuations.

2.3 Notation and physical regimes

We use Gaussian electromagnetic units throughout. $\boldsymbol{B}$ is the *physical* magnetic field in gauss, $\boldsymbol{U}$ the bulk velocity, ρ the mass density, and $e > 0$ the elementary charge. Temperature T is in kelvin, with $k_B T$ written explicitly; temperatures quoted in eV refer to $k_B T$. The magnetic diffusivity is $\eta = c^2/(4\pi\sigma)$, with dimensions length squared per time, and ν is kinematic viscosity.

The battery calculation uses a scalar electron pressure. The Weibel calculations use an unmagnetized collisionless kinetic or cold-fluid model. The classical dynamo calculation later uses resistive MHD at constant density. We will identify the assumptions at each transition; magnetization by a seed does not by itself establish a collisional MHD closure.

3 The Biermann battery

3.1 From the electron force balance to a magnetic source

For sufficiently slow electron dynamics, neglect electron inertia. Retaining a simple electron–ion collision force, the electron momentum balance is

$$0 = -en_e\left(\boldsymbol{E} + \frac{\boldsymbol{U}_e \times \boldsymbol{B}}{c}\right) - \boldsymbol{\nabla} p_e + \boldsymbol{R}_{ei}. \tag{3.1}$$

Here $\boldsymbol{R}_{ei}$ is the force per unit volume exerted on electrons by collisions with ions. In a scalar friction model,

$$\boldsymbol{R}_{ei} = m_e n_e \nu_{ei}(\boldsymbol{U}_i - \boldsymbol{U}_e), \qquad \boldsymbol{J} = en_e(\boldsymbol{U}_i - \boldsymbol{U}_e),$$

where quasineutrality and singly charged ions have been assumed. Thus

$$\frac{\boldsymbol{R}_{ei}}{en_e} = \frac{m_e \nu_{ei}}{n_e e^2}\boldsymbol{J} \equiv \frac{\boldsymbol{J}}{\sigma}, \qquad \sigma = \frac{n_e e^2}{m_e \nu_{ei}}.$$

Rearranging the momentum balance gives *Ohm's law in terms of the electron velocity*:

$$\boldsymbol{E} + \frac{\boldsymbol{U}_e \times \boldsymbol{B}}{c} = -\frac{\boldsymbol{\nabla} p_e}{en_e} + \frac{\boldsymbol{J}}{\sigma}.$$

The left-hand side is the electric field in the local electron-fluid frame, to nonrelativistic accuracy. It balances the electron pressure force and collisional friction per unit charge. The resistive term therefore comes from collisions; it would be absent if $\boldsymbol{R}_{ei}$ had been omitted from the starting equation.

To express this law in terms of the bulk velocity, use the mass-weighted velocity and the current relation:

$$\boldsymbol{U} = \frac{m_i \boldsymbol{U}_i + m_e \boldsymbol{U}_e}{m_i + m_e} \simeq \boldsymbol{U}_i, \qquad \boldsymbol{U}_e = \boldsymbol{U}_i - \frac{\boldsymbol{J}}{en_e} \simeq \boldsymbol{U} - \frac{\boldsymbol{J}}{en_e}.$$

The approximation uses $m_e \ll m_i$; it does not set the electron and ion velocities equal. Substituting into the electron motional term,

$$\frac{\boldsymbol{U}_e \times \boldsymbol{B}}{c} \simeq \frac{\boldsymbol{U} \times \boldsymbol{B}}{c} - \frac{\boldsymbol{J} \times \boldsymbol{B}}{en_e c},$$

and moving the current term to the right gives the generalized Ohm's law in the bulk-fluid frame:

$$\boldsymbol{E} + \frac{\boldsymbol{U} \times \boldsymbol{B}}{c} = \frac{\boldsymbol{J} \times \boldsymbol{B}}{en_e c} - \frac{\boldsymbol{\nabla} p_e}{en_e} + \frac{\boldsymbol{J}}{\sigma}. \tag{3.2}$$

The Hall term matters in suitable magnetized, small-scale regimes. It vanishes at $\boldsymbol{B} = 0$, so it is not the source studied here. Omitting it for this calculation, Faraday's law gives

$$\frac{\partial \boldsymbol{B}}{\partial t} = \boldsymbol{\nabla} \times (\boldsymbol{U} \times \boldsymbol{B}) + \eta \nabla^2 \boldsymbol{B} + \frac{c}{e} \boldsymbol{\nabla} \times \left(\frac{\boldsymbol{\nabla} p_e}{n_e} \right), \tag{3.3}$$

$$\boldsymbol{\nabla} \times \left(\frac{\boldsymbol{\nabla} p_e}{n_e} \right) = \boldsymbol{\nabla} \left(\frac{1}{n_e} \right) \times \boldsymbol{\nabla} p_e = -\frac{\boldsymbol{\nabla} n_e \times \boldsymbol{\nabla} p_e}{n_e^2}. \tag{3.4}$$

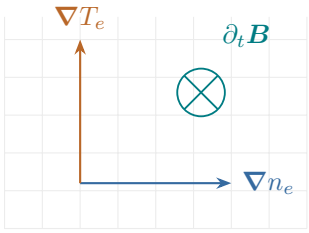
With $p_e = n_e k_B T_e$, the resulting equation is

$$\frac{\partial \boldsymbol{B}}{\partial t} = \boldsymbol{\nabla} \times (\boldsymbol{U} \times \boldsymbol{B}) + \eta \nabla^2 \boldsymbol{B} + \underbrace{\frac{c k_B}{e n_e} \boldsymbol{\nabla} T_e \times \boldsymbol{\nabla} n_e}_{\text{Biermann source}}. \tag{3.5}$$

The pressure force per electron need not be the gradient of a single scalar potential: spatially varying $1/n_e$ makes its curl nonzero. Faraday's law then generates a magnetic field. If p_e is a function of n_e alone, the two gradients are parallel and the source vanishes. A temperature gradient alone, in a strictly uniform-density plasma, also gives no scalar-pressure Biermann source.

3.2 Geometry, direction, and the vorticity analogy

The generated field is perpendicular to both gradients. For example, $\boldsymbol{\nabla} T_e$ along $+\hat{\boldsymbol{y}}$ and $\boldsymbol{\nabla} n_e$ along $+\hat{\boldsymbol{x}}$ generate $\partial_t \boldsymbol{B}$ along $-\hat{\boldsymbol{z}}$, into the page.



Misaligned thermodynamic gradients produce a rotational electric field. The sign follows $\boldsymbol{\nabla} T_e \times \boldsymbol{\nabla} n_e$.

Figure 4: The local battery geometry. The cross marks a field growing into the page. Reversing either gradient reverses the source.

There is a close analogy with baroclinic vorticity generation in an ordinary fluid. Taking the curl of $-(1/\rho)\boldsymbol{\nabla} p$ gives

$$\left. \frac{\partial \boldsymbol{\omega}}{\partial t} \right|_{\text{baroclinic}} = \frac{\boldsymbol{\nabla} \rho \times \boldsymbol{\nabla} p}{\rho^2}, \qquad \boldsymbol{\omega} = \boldsymbol{\nabla} \times \boldsymbol{U}. \tag{3.6}$$

Both effects require misaligned thermodynamic gradients. The analogy explains why curved shocks, expanding heated regions, and nonuniform structures are natural sites to look for battery generation. It does not make electron pressure and total-fluid pressure interchangeable.

3.3 How much field is produced?

Define $L_T = T_e/|\boldsymbol{\nabla} T_e|$, $L_n = n_e/|\boldsymbol{\nabla} n_e|$, and let θ be the angle between the gradients. If the gradients remain roughly fixed during a time t, then

$$B_{\text{seed}} \sim \frac{c k_B T_e}{e L_T L_n} \, t \, |\sin \theta|. \tag{3.7}$$

This is a generation estimate, before significant modification by transport, changing gradients, or feedback. It immediately explains the contrast between diffuse cosmic systems and compact laser plasmas:

$$B_{\rm seed} \sim 1.7\times10^{-20}\,{\rm G}\,\frac{k_B T_e}{5\,{\rm keV}}\frac{t}{10^8\,{\rm yr}}\frac{(100\,{\rm kpc})^2}{L_T L_n}|\sin\theta|, \tag{3.8}$$

$$B_{\rm seed} \sim 10^{6}\,{\rm G}\,\frac{k_B T_e}{1\,{\rm keV}}\frac{t}{1\,{\rm ns}}\frac{(100\,\mu{\rm m})^2}{L_T L_n}|\sin\theta|. \tag{3.9}$$

These are illustrative parameter choices, not universal cosmic or laboratory field strengths. Small gradient scales can make a battery field large in gauss even over a nanosecond. The comparison with the pressure, particle orbits, and system size is still needed to assess its importance.

3.4 When does induction compete with the battery?

For $L_T \sim L_n \sim L$, order-unity misalignment, and flow speed U, compare the source with $\boldsymbol{\nabla}\times(\boldsymbol{U}\times\boldsymbol{B}) \sim UB/L$:

$$\frac{\text{battery}}{\text{induction}} \sim \frac{ck_BT_e}{eUBL}, \qquad B_{\rm cross} \sim \frac{ck_BT_e}{eUL}. \tag{3.10}$$

The source is independent of the existing field, whereas induction increases with B. For a hydrogen plasma, introduce

$$c_s = \sqrt{\frac{k_BT_e}{m_i}}, \quad \Omega_i = \frac{eB}{m_ic}, \quad \rho_s = \frac{c_s}{\Omega_i}, \quad d_i = \frac{c}{\sqrt{4\pi n_i e^2/m_i}}. \tag{3.11}$$

Here c_s is an electron-pressure sound-speed scale, not a general expression for the full sound speed. Equation (3.10) becomes

$$\frac{\text{battery}}{\text{induction}} \sim \frac{c_s}{U}\frac{\rho_s}{L}. \tag{3.12}$$

For $U \sim c_s$, the crossover occurs at $\rho_s \sim L$, and

$$\beta_e(B_{\rm cross}) \equiv \frac{8\pi n_e k_B T_e}{B_{\rm cross}^2} \sim 2\left(\frac{L}{d_i}\right)^2. \tag{3.13}$$

Thus the battery can hand over to inductive evolution while the field is still energetically very weak in a large system. Equality of these two estimates is *not a saturation condition*: subsequent stretching may amplify the field, and changing gradients or transport may alter the battery itself [6].

3.5 Laser-produced fields and their reconnection

A laser-heated spot expands into a nonuniform plasma. Density and temperature contours need not coincide, so the battery produces a field that circles the expanding plume. Adjacent heated regions can bring oppositely directed fields together and form a reconnecting layer. This supplies a direct connection to the previous topic: a seed-generation mechanism can create the field geometry used in a reconnection experiment.

Proton radiography infers electromagnetic structure from the deflections of probing protons. It measures a projected deflection pattern, so interpreting it as a local magnetic-field map requires a model of geometry and possible electric fields. Megagauss self-generated fields and rapid transport have been studied experimentally; strong heat fluxes can transport magnetic flux through the Nernst effect faster than the ion bulk flow [8]. Two-beam laser experiments also probe the collision of magnetized plumes and reconnection [9]. The simple battery equation explains a source, but is not by itself a complete model of a laser plasma.

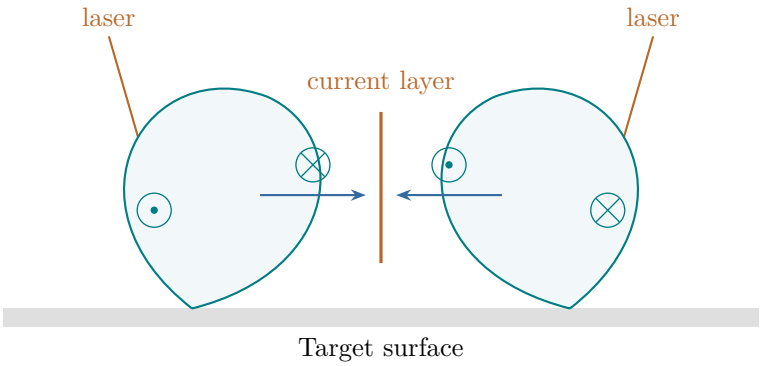


Figure 5: A cross-section through two laser-heated plumes, with azimuthal battery fields represented by dots and crosses. The inner flanks carry opposite field directions. Arrows show expansion toward the interaction layer; the sketch does not specify the detailed field-transport mechanism.

4 Weibel Instability

4.1 Thermal Weibel Instability

The equilibrium and the source of free energy

Consider a homogeneous, initially unmagnetized electron plasma with stationary neutralizing ions. Choose a wavevector along $\hat{\boldsymbol{z}}$ and an equilibrium distribution

$$f_0(\boldsymbol{v}) = \frac{n_0}{\pi^{3/2} v_\perp^2 v_\parallel} \exp\left[-\frac{v_x^2 + v_y^2}{v_\perp^2} - \frac{v_z^2}{v_\parallel^2}\right], \qquad v_{\perp,\parallel}^2 = \frac{2k_B T_{\perp,\parallel}}{m_e}. \tag{4.1}$$

The labels $\parallel$ and $\perp$ refer to the chosen symmetry axis and wavevector, *not* a background magnetic field. Define

$$\Delta = \frac{T_\perp}{T_\parallel} - 1, \qquad \omega_{pe}^2 = \frac{4\pi n_0 e^2}{m_e}, \qquad d_e = \frac{c}{\omega_{pe}}. \tag{4.2}$$

We study $\Delta > 0$: the electrons have more random kinetic energy across the wavevector than along it. No net current is required in the equilibrium.

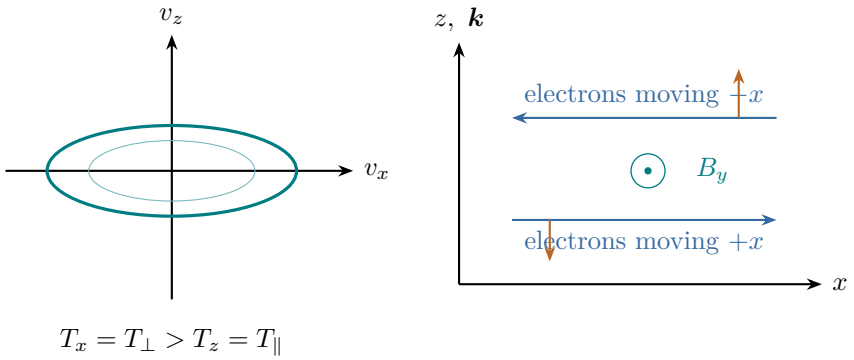


Figure 6: Left: a contour of the bi-Maxwellian in the v_x–v_z plane. Right: opposite v_x populations are deflected in opposite z directions by a magnetic perturbation. With x right and z up, $+y$ points out of the page. The resulting current modulation can reinforce the magnetic perturbation.

A small $B_y(z)$ deflects oppositely moving electrons in opposite transverse directions. Their redistribution produces a modulated current along x, which can reinforce the field. Motion along z tends to wash out this separation. The instability is the result of this competition; an isotropic Maxwellian does not provide the required anisotropic free energy [10, 11].

The magnetic force changes particle direction but does no work. Energy transfer to the growing electromagnetic perturbation occurs through the electric field and $\boldsymbol{J}\cdot\boldsymbol{E}$. Calling the instability "magnetic" does not mean that its electric perturbation may be discarded from an energy argument.

A short kinetic derivation

Take perturbations proportional to $\exp(ikz - i\omega t)$, with $\boldsymbol{E}_1 = E_x\hat{\boldsymbol{x}}$ and $\boldsymbol{B}_1 = B_y\hat{\boldsymbol{y}}$. Faraday's law gives

$$B_y = \frac{ck}{\omega}E_x. \tag{4.3}$$

For electron charge $q_e = -e$, the linearized Vlasov equation is

$$-i(\omega - kv_z)f_1 + \frac{q_e}{m_e}\left[\left(E_x - \frac{v_z B_y}{c}\right)\frac{\partial f_0}{\partial v_x} + \frac{v_x B_y}{c}\frac{\partial f_0}{\partial v_z}\right] = 0. \tag{4.4}$$

Substituting Faraday's law and collecting terms gives

$$f_1 = -\frac{iq_eE_x}{m_e\omega}\left[\frac{\partial f_0}{\partial v_x} + \frac{kv_x}{\omega - kv_z}\frac{\partial f_0}{\partial v_z}\right]. \tag{4.5}$$

Now compute $J_x = q_e\int v_x f_1\,\mathrm{d}^3v$. The first term integrates by parts to $-n_0$. In the second, the Gaussian v_x integral supplies $\langle v_x^2\rangle = v_\perp^2/2$, leaving the one-dimensional response along z:

$$k\int \frac{v_x^2}{\omega - kv_z}\frac{\partial f_0}{\partial v_z}\,\mathrm{d}^3v = n_0\frac{T_\perp}{T_\parallel}\left[1 + \xi Z(\xi)\right], \qquad \xi = \frac{\omega}{kv_\parallel}. \tag{4.6}$$

The plasma dispersion function is

$$Z(\xi) = \frac{1}{\sqrt{\pi}}\int_{-\infty}^{\infty}\frac{e^{-s^2}}{s-\xi}\,\mathrm{d}s, \qquad \operatorname{Im}\xi > 0, \tag{4.7}$$

with analytic continuation for other frequencies. Thus

$$J_x = \frac{i\omega_{pe}^2}{4\pi\omega}\left\{1 - (1+\Delta)[1 + \xi Z(\xi)]\right\}E_x. \tag{4.8}$$

Ampère–Maxwell gives the same current as

$$J_x = \frac{i}{4\pi\omega}(\omega^2 - c^2k^2)E_x. \tag{4.9}$$

Equating the two expressions yields

$$\omega^2 - c^2k^2 + \omega_{pe}^2\left[\Delta + (1+\Delta)\xi Z(\xi)\right] = 0. \tag{4.10}$$

This is the transverse electron-Weibel dispersion relation for the stated bi-Maxwellian and immobile-ion model. The two transverse polarizations are equivalent because $T_x = T_y$.

Unstable wavelengths and the familiar scalings

Look for a nonpropagating growing mode, $\omega = i\gamma$ with $\gamma > 0$. At marginal stability, $\gamma \to 0$, equation (4.10) gives

$$k^2d_e^2 = \Delta. \tag{4.11}$$

The unstable band is $0 < kd_e < \sqrt{\Delta}$. For weak anisotropy, $\gamma/(kv_\parallel) \ll 1$, use $Z(\xi) \simeq i\sqrt{\pi} - 2\xi$. Dropping γ^2/ω_{pe}^2 at nonrelativistic thermal speed gives

$$\gamma(k) \simeq \frac{kv_\parallel}{\sqrt{\pi}(1+\Delta)}\left(\Delta - k^2 d_e^2\right). \tag{4.12}$$

The derivative of $k(\Delta - k^2 d_e^2)$ vanishes at $3k^2 d_e^2 = \Delta$. Therefore

$$k_{\max} d_e \simeq \sqrt{\frac{\Delta}{3}}, \qquad \frac{\gamma_{\max}}{\omega_{pe}} \simeq \frac{2}{3\sqrt{3\pi}} \frac{v_\parallel}{c} \frac{\Delta^{3/2}}{1+\Delta}. \tag{4.13}$$

These display the useful weak-anisotropy scalings $kd_e \propto \Delta^{1/2}$ and $\gamma \propto \Delta^{3/2}$. The thermal-speed factor $v_\parallel/c$ is essential when normalizing the growth rate to ω_{pe}. The unstable structures need not have width exactly d_e; their characteristic inverse wavenumber increases as the anisotropy decreases.

What stops the initial growth?

The linear calculation assumes the original f_0 remains unchanged. Growing magnetic structure bends particle orbits, creates magnetic trapping, and redistributes the anisotropy. A useful trapping estimate follows by expanding the transverse force near a stable point of a sinusoidal field:

$$\omega_b^2 \sim kv_\perp \Omega_e, \qquad \Omega_e = \frac{eB}{m_e c}. \tag{4.14}$$

The condition $\omega_b \sim \gamma$ estimates when trapped orbits can modify the linear response. Another useful measure is r_{Le}/λ_B, which asks whether particles can turn substantially within a magnetic structure. These criteria describe related orbit changes, but are not interchangeable universal saturation formulas. Continued anisotropy driving, mode merging, and species response can change the outcome.

Collisions compete by relaxing the distribution. For a fixed anisotropic equilibrium, a collisionless growth estimate requires the relevant relaxation rate to be small compared with the growth rate. In a driven system one must also compare collisions with the rate at which anisotropy is produced. The condition $\nu_{ee} L/v_{te} \ll 1$ diagnoses nearly free streaming across a gradient, but alone does not guarantee that a slowly growing Weibel mode survives [7].

4.2 Counter-streaming Beams

The Weibel instability can also be understood by considering two counter-streaming electron populations, providing a simple complement to the bi-Maxwellian description [11]. Two equal populations moving in opposite directions have zero net current, yet their combined velocity distribution is anisotropic. A small transverse magnetic perturbation deflects the populations in opposite directions and can produce a reinforcing current modulation.

The cold-beam derivation is left as a Homework 3 exercise, *Counter-streaming Weibel instability*. Starting from separate continuity and momentum equations for the two electron populations, the exercise derives the electromagnetic dispersion relation and growth rate, then compares the result with thermal Weibel and discusses its kinetic character.

Discussion. The anisotropy can be created in several ways: counter-streaming laser plasmas produce ion-scale Weibel structure [12], optically ionized plasmas allow direct tests of thermal electron-Weibel growth [13], and kinetic simulations show that expansion can generate anisotropy and magnetic filaments [14]. In expanding plasmas, Biermann fields from misaligned macroscopic gradients can coexist with Weibel fields; their relative importance depends on collisionality, anisotropy, and coherence scale, as well as field strength [6, 7]. Filamentation also provides a possible source of magnetic fields in collisionless

shocks [15]. Anisotropy need not be imposed initially: in a weakly collisional shear flow, free-streaming particles sample regions with different mean velocities, producing unequal principal pressures. A kinetic study follows this sequence from large-scale shear to pressure anisotropy, Weibel growth, and modification of particle orbits by the generated field [16]. Its scaling tests use electron–positron plasmas. This offers a concrete route by which macroscopic motions generate microscopic magnetic seeds; their later amplification and survival require following the evolving flow and its magnetic feedback.

5 From a seed field to dynamo amplification

5.1 The question changes: can the field keep growing?

Biermann and Weibel processes explain how a seed field can appear. Once a seed exists, a different question arises: will stirring amplify it faster than magnetic diffusion removes it? We begin with forced, three-dimensional turbulence and a dynamically weak field. The flow is initially approximately hydrodynamic; there is no imposed strong guide field on which to base an Alfvénic cascade.

In the *kinematic approximation*, magnetic feedback on the velocity is negligible. For incompressible flow of constant density ρ and constant magnetic diffusivity η, the induction equation is

$$\frac{D\boldsymbol{B}}{Dt} = (\boldsymbol{B}\cdot\boldsymbol{\nabla})\boldsymbol{U} + \eta\nabla^2\boldsymbol{B}, \qquad \frac{D}{Dt} = \frac{\partial}{\partial t} + \boldsymbol{U}\cdot\boldsymbol{\nabla}. \tag{5.1}$$

The material derivative follows the moving fluid. The first term on the right describes deformation of the field by velocity gradients; its stretching part can increase the field strength. The second smooths magnetic structure. We retain $\boldsymbol{B}$ in physical, Gaussian-cgs units throughout these sections.

A *small-scale*, or *fluctuation*, dynamo amplifies magnetic fluctuations on scales at or below the driving scale L. A field with oppositely directed patches can have

$$\langle\boldsymbol{B}\rangle = 0 \qquad \text{while} \qquad \left\langle B^2\right\rangle \text{ grows.}$$

Indeed, the volume-averaged field is conserved in a periodic box, but magnetic energy need not be. Net kinetic helicity is not required. Producing an organized mean field on scales larger than the driving eddies is the separate mean-field-dynamo problem.

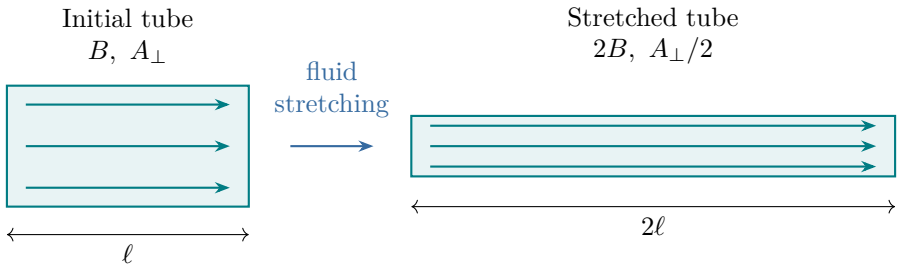
Regime used below. Our main small-scale-dynamo discussion, including the nonlinear stage, concerns *large magnetic Prandtl number*, $\mathrm{Pm} \equiv \nu/\eta \gg 1$, where ν is the kinematic viscosity. This regime is relevant to hot, dilute astrophysical plasmas such as the intracluster medium (ICM). For $T \sim 10^8\,\mathrm{K}$ and $n \sim 10^{-3}\,\mathrm{cm}^{-3}$, classical Spitzer transport coefficients give $\mathrm{Pm} \sim 2\times10^{29}$ [33, Section 2.6.3]. This is a classical estimate; effective transport in a weakly collisional, magnetized plasma can differ. The essential ordering here is $\ell_\eta \ll \ell_\nu$: magnetic structure survives below the smallest turbulent eddies. Low-Pm systems, including stellar convection zones and planetary interiors [24], receive only a brief comparison in Section 6.4.

5.2 Stretching a flux tube: where the energy comes from

Consider a thin material flux tube while diffusion is negligible. Flux freezing conserves its magnetic flux, and incompressibility conserves its volume. If its cross-sectional area is $A_\perp$ and its length is ℓ, then

$$BA_\perp = \text{const}, \qquad A_\perp\ell = \text{const} \quad\Longrightarrow\quad B \propto \ell. \tag{5.2}$$

Stretching the tube makes it thinner and strengthens its field. The flow does work against magnetic tension: the extra magnetic energy comes from kinetic energy, ultimately supplied by the forcing.



Ideal, incompressible deformation: the same flux in a smaller cross section.

Figure 7: A flux tube gains field strength when stretched. The drawing represents a tube with fixed depth into the page, so halving its drawn width halves its cross-sectional area. Repeated stretching must still compete with diffusion to produce a sustained dynamo.

With periodic boundaries or vanishing surface fluxes, the magnetic energy $E_B = \int_V B^2/(8\pi)\,\mathrm{d}V$ obeys

$$\frac{\mathrm{d}E_B}{\mathrm{d}t} = \underbrace{\frac{1}{4\pi}\int_V \boldsymbol{B}\cdot[(\boldsymbol{B}\cdot\boldsymbol{\nabla})\boldsymbol{U}]\,\mathrm{d}V}_{\text{work by the flow}} - \underbrace{\frac{\eta}{4\pi}\int_V |\boldsymbol{\nabla}\times\boldsymbol{B}|^2\,\mathrm{d}V}_{\text{Ohmic loss}}. \tag{5.3}$$

Stretching creates both stronger field and sharper gradients. The first increases the energy supply; the second makes diffusion more effective. A dynamo requires positive net work after this loss is included.

5.3 Why a single stretch is not yet a dynamo

On the driving scale, define

$$\mathrm{Rm} = \frac{UL}{\eta}, \qquad \mathrm{Re} = \frac{UL}{\nu}, \qquad \mathrm{Pm} = \frac{\nu}{\eta} = \frac{\mathrm{Rm}}{\mathrm{Re}}. \tag{5.4}$$

Rm compares induction with magnetic diffusion, whereas Re compares fluid inertia with viscosity. Turbulence in a poorly conducting fluid need not amplify magnetic fields. The dynamo threshold is a critical Rm that depends on the flow, boundaries, and Pm, rather than a universal critical Re.

A single stretch can strengthen a flux tube, but sustained dynamo action requires the flow to keep supplying magnetic energy in spite of diffusion. Stretching also makes thinner structures, which diffuse faster. Geometry therefore matters as well as Rm: a flow can produce temporary amplification while failing to regenerate the field needed for continued growth. The following two anti-dynamo theorems make this distinction concrete.

5.4 The planar anti-dynamo theorem

Take incompressible flow $\boldsymbol{U} = (U_x, U_y, 0)$, with all quantities independent of z, constant magnetic diffusivity $\eta > 0$, and no imposed mean magnetic flux. Write the in-plane field as

$$\boldsymbol{B}_\perp = \boldsymbol{\nabla}\times(A\hat{\boldsymbol{z}}) = (\partial_y A, -\partial_x A, 0). \tag{5.5}$$

Here A is the magnetic flux function, distinct from the tube area $A_\perp$. The induction equation reduces to

$$\frac{\partial A}{\partial t} + \boldsymbol{U}_\perp\cdot\boldsymbol{\nabla}_\perp A = \eta\nabla_\perp^2 A. \tag{5.6}$$

Multiply by A and integrate over the plane. For periodic boundaries, or an impermeable boundary where $A = 0$, the contribution from U_x, U_y is exactly a vanishing boundary term:

$$\begin{aligned} -\int A\,\boldsymbol{U}_\perp \cdot \boldsymbol{\nabla}_\perp A\,\mathrm{d}^2x &= -\frac{1}{2}\int \boldsymbol{U}_\perp \cdot \boldsymbol{\nabla}_\perp (A^2)\,\mathrm{d}^2x \\ &= -\frac{1}{2}\int \boldsymbol{\nabla}_\perp \cdot (\boldsymbol{U}_\perp A^2)\,\mathrm{d}^2x = 0. \end{aligned}$$

The second equality uses $\boldsymbol{\nabla}_\perp \cdot \boldsymbol{U}_\perp = 0$. Integrating the diffusion term by parts then gives

$$\frac{\mathrm{d}}{\mathrm{d}t}\int \frac{A^2}{2}\,\mathrm{d}^2x = -\eta\int |\boldsymbol{\nabla}_\perp A|^2\,\mathrm{d}^2x = -\eta\int |\boldsymbol{B}_\perp|^2\,\mathrm{d}^2x. \tag{5.7}$$

No choice of the two-dimensional U_x, U_y can increase $\int A^2\,\mathrm{d}^2x$ under these assumptions. They redistribute A but provide no net contribution to this integral. If the in-plane magnetic energy remained bounded away from zero indefinitely, the right-hand side of (5.7) would eventually drive the nonnegative quantity $\int A^2/2$ below zero. Thus the field cannot be maintained indefinitely. The out-of-plane component B_z also obeys advection–diffusion; it need not be set to zero. For smooth bounded flows and the stated boundary conditions, no sustained dynamo is possible [18].

This does not forbid transient magnetic amplification: the decreasing quantity is $\int A^2$, whereas magnetic energy depends on $\int |\boldsymbol{\nabla}_\perp A|^2$.

What changes when three-dimensional coupling is allowed? Return to the full incompressible induction equation, with $D/Dt = \partial_t + \boldsymbol{U}\cdot\boldsymbol{\nabla}$:

$$\frac{D\boldsymbol{B}_\perp}{Dt} = (\boldsymbol{B}_\perp \cdot \boldsymbol{\nabla}_\perp)\boldsymbol{U}_\perp + \underbrace{B_z\partial_z \boldsymbol{U}_\perp}_{B_z\ \to\ \boldsymbol{B}_\perp} + \eta\nabla^2\boldsymbol{B}_\perp,$$

$$\frac{DB_z}{Dt} = \underbrace{\boldsymbol{B}_\perp \cdot \boldsymbol{\nabla}_\perp U_z}_{\boldsymbol{B}_\perp\ \to\ B_z} + B_z\partial_z U_z + \eta\nabla^2 B_z.$$

Both underbraced terms vanish in the original setup. Allowing U_z to vary in x, y permits an in-plane field to generate B_z through $B_x\partial_x U_z + B_y\partial_y U_z$. Allowing U_x, U_y to vary in z lets B_z generate in-plane field through $B_z\partial_z \boldsymbol{U}_\perp$. These are concrete channels for two-way coupling between the field components.

Merely adding a nonzero U_z or B_z while keeping all fields independent of z does not supply the missing feedback to the A equation. With general three-dimensional structure, $\boldsymbol{\nabla}_\perp \cdot \boldsymbol{B}_\perp = -\partial_z B_z$, so a single planar flux function $A(x, y)$ no longer describes the field and the preceding scalar proof does not apply. The displayed coupling is one way to remove this geometric restriction; it does not by itself guarantee dynamo growth, which still requires induction to overcome diffusion [24].

5.5 Cowling's theorem: axisymmetry cannot sustain the field

Cowling's theorem rules out self-maintenance of an axisymmetric magnetic field under the usual resistive-MHD, isolated-system assumptions [19]. A useful demonstration takes both velocity and magnetic field axisymmetric in cylindrical coordinates (R, ϕ, z), so $\partial/\partial\phi = 0$, and separates poloidal and toroidal components:

$$\boldsymbol{B} = \boldsymbol{B}_p + B_\phi\hat{\boldsymbol{\phi}}, \quad \boldsymbol{U} = \boldsymbol{U}_p + R\Omega\hat{\boldsymbol{\phi}}, \quad \boldsymbol{B}_p = \frac{1}{R}\boldsymbol{\nabla}\psi \times \hat{\boldsymbol{\phi}}. \tag{5.8}$$

The poloidal components lie in the (R, z) plane; the toroidal components point around the symmetry axis. Here Ω is the angular velocity and $2\pi\psi$ is the poloidal magnetic flux through a circle of radius R, measured from the axis. The poloidal flux evolves as

$$\frac{\partial\psi}{\partial t} + \boldsymbol{U}_p \cdot \boldsymbol{\nabla}\psi = \eta\left(\frac{\partial^2\psi}{\partial R^2} - \frac{1}{R}\frac{\partial\psi}{\partial R} + \frac{\partial^2\psi}{\partial z^2}\right). \tag{5.9}$$

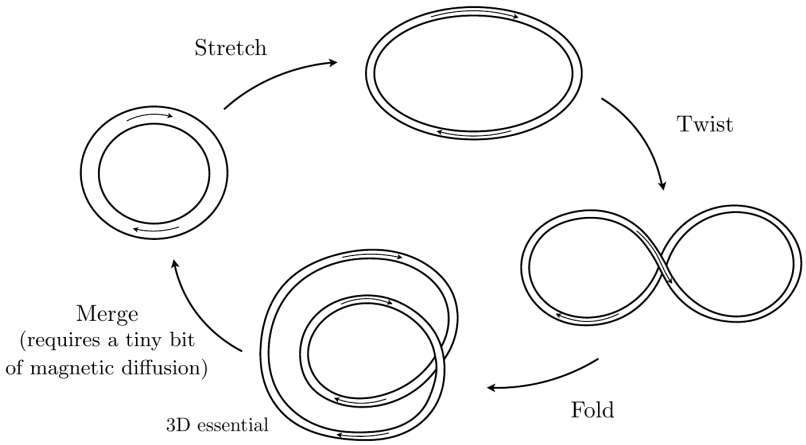
It has transport and diffusion, but no source from B_ϕ. Differential rotation does create a toroidal field, through a term $R\boldsymbol{B}_p \cdot \boldsymbol{\nabla}\Omega$ in its induction equation. Once the unsustained poloidal field decays, this toroidal source disappears. Winding can amplify the field temporarily, but the amplification loop is not closed: the toroidal field cannot regenerate the poloidal field within this axisymmetric system.

The restriction is on sustaining an axisymmetric *field*. It does not say that every axisymmetric velocity field is incapable of exciting a non-axisymmetric magnetic field. Nor does it prohibit an observed field from having a substantial axisymmetric mean component when three-dimensional fluctuations are present.

Together, these examples explain why repeated stretching, reorientation, and the three-dimensional arrangement of the field matter. Three-dimensionality evades these particular restrictions but is not, by itself, a proof of dynamo action. We next use a physical model of random stretching and check its growth, geometry, and energy budget.

6 Kinematic turbulent dynamo: rates, folds, and spectra

Zel'dovich's *stretch–twist–fold* picture shows how stretching can be repeated within a bounded region. He demonstrated the idea at the 1967 IAU meeting in Prague [32]; a classical published account is Vainshtein and Zel'dovich [31].



(a) Stretch, twist, fold, and repeat



(b) Zel'dovich, Prague, 1967

Figure 8: Zel'dovich's stretch–twist–fold dynamo. (a) The amplification cycle, reproduced from Rincon [24, Figure 9]. (b) Zel'dovich demonstrating the idea at the 1967 IAU meeting. Photograph by Leo Goldberg, courtesy AIP Emilio Segrè Visual Archives; reproduced from Shukurov, Sokoloff, and Schekochihin [32, Figure 1].

Stretching doubles the tube's length and field strength at fixed volume and flux. A three-dimensional twist and fold place the two loops alongside one another with their fields aligned; weak magnetic diffusion allows them to merge so that the cycle can repeat [31, 24]. The flow supplies the magnetic energy. This idealized cycle motivates repeated amplification; the turbulent field geometry and its reversal scale are described below.

6.1 Which eddies stretch the field fastest?

The classical question of magnetic amplification by homogeneous turbulence goes back to Batchelor [27]. For the high-Pm kinematic picture developed below, Schekochihin et al. [20] connect the stretching estimates to simulations, field geometry, and spectra.

A large eddy has a large velocity, but magnetic amplification responds to a *velocity difference across a distance*. Using the Kolmogorov estimate from hydrodynamic turbulence,

$$\delta U_\ell \sim (\epsilon \ell)^{1/3}, \qquad \tau_\ell^{-1} \sim \frac{\delta U_\ell}{\ell} \sim \epsilon^{1/3} \ell^{-2/3}. \tag{6.1}$$

Here ϵ is the turbulent energy transfer rate per unit mass and $\tau_\ell \sim \ell/\delta U_\ell$ is the eddy turnover time. Its inverse estimates the stretching rate. Smaller inertial-range eddies have smaller speeds but shorter turnover times, so they stretch the field faster.

Viscosity cuts off this sequence. Recall the hydrodynamic estimates

$$\ell_\nu \sim L\mathrm{Re}^{-3/4}, \qquad \delta U_{\ell_\nu} \sim U\mathrm{Re}^{-1/4}, \qquad \tau_\nu^{-1} \sim \frac{U}{L}\mathrm{Re}^{1/2}. \tag{6.2}$$

Here $\tau_\nu \equiv \tau_{\ell_\nu}$ is the viscous-scale turnover time. Below ℓ_ν, the velocity is smooth: $\delta U_\ell \sim \ell/\tau_\nu$. Its strain no longer increases as the separation is reduced (Figure 9). In high-Pm kinematic dynamo, the magnetic-energy growth rate is of order τ_ν^{-1}. Thus amplification can be much faster than the turnover of the driving eddies, provided dynamo is excited [20].

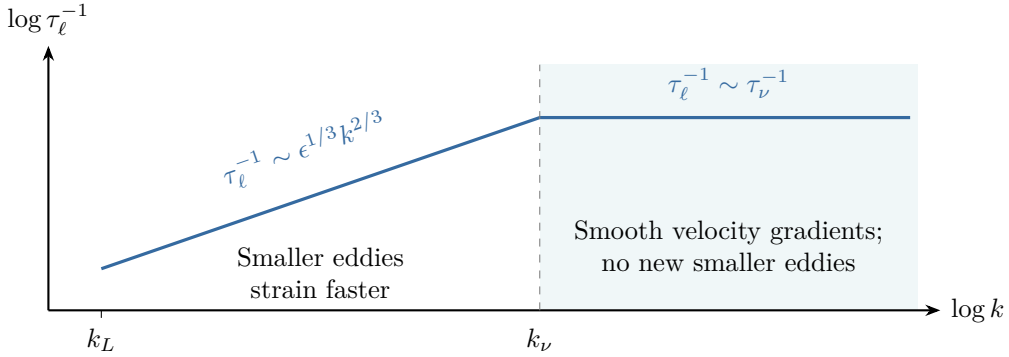


Figure 9: Stretching rate τ_ℓ^{-1} sampled at separation $\ell \sim k^{-1}$. The plateau denotes the same smooth velocity gradient sampled across smaller distances; it is not a spectrum of independent subviscous eddies. The schematic illustrates the Kolmogorov strain estimates used in the high-Pm dynamo picture [20]; it is not simulation data.

The rate estimates identify the relevant motions, not a guarantee of growth. Whether net stretching wins over diffusion also depends on field orientation and the history of the strain. In the kinematic growing regime we write $E_B \propto e^{\gamma_E t}$, using γ_E for the *energy* growth rate; B_{rms} then grows at rate $\gamma_E/2$.

6.2 What does the amplified field look like?

Successive deformations stretch, reorient, and fold the seed. A characteristic high-Pm structure consists of long, nearly straight stretches of strong field, with neighboring stretches pointing in opposite directions [20]. Two different lengths are needed to describe it: the distance over which the field varies along a stretch, and the much smaller transverse distance over which its direction reverses.

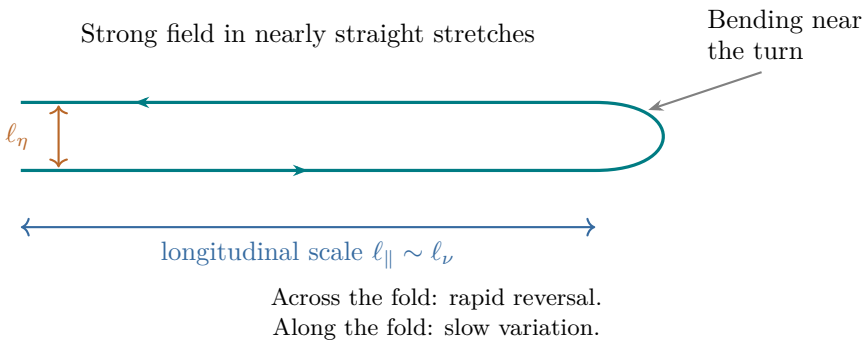


Figure 10: A folded field in the high-Pm kinematic picture; the transverse spacing is exaggerated. The long straight portions and the narrow separation are different geometric features. Strong curvature is localized near turns, where the field can be weaker. Later, the stretching and longitudinal scales can grow beyond ℓ_ν. This schematic illustrates the folded-field geometry studied by Schekochihin et al. [20]; see also Schekochihin [30, Section 13.1].

Magnetic reversal at a short transverse scale does not require a velocity eddy at that same scale. A smooth flow can stretch a pattern into progressively thinner strips. This distinction will also matter for the magnetic tension that eventually reacts back on the flow.

6.3 High magnetic Prandtl number: two different cutoffs

For $\mathrm{Pm} \gg 1$, viscosity smooths the velocity before resistivity smooths the magnetic field. Stretching by the smooth viscous-scale flow produces smaller magnetic reversals until diffusion competes with that stretching:

$$\frac{\eta}{\ell_\eta^2} \sim \tau_\nu^{-1} \sim \frac{\nu}{\ell_\nu^2}. \tag{6.3}$$

Therefore

$$\ell_\eta \sim \ell_\nu \mathrm{Pm}^{-1/2}, \qquad \ell_\eta \ll \ell_\nu \ll L, \qquad \gamma_E \sim \tau_\nu^{-1}. \tag{6.4}$$

The growth rate is set by the stretching flow, while the finest magnetic scale is set by diffusion. Extrapolating $\delta U_\ell \propto \ell^{1/3}$ below ℓ_ν would use an inertial-range formula where the velocity is already smooth. These separated viscous and resistive scales are central to the high-Pm theory and simulations in Schekochihin et al. [20].

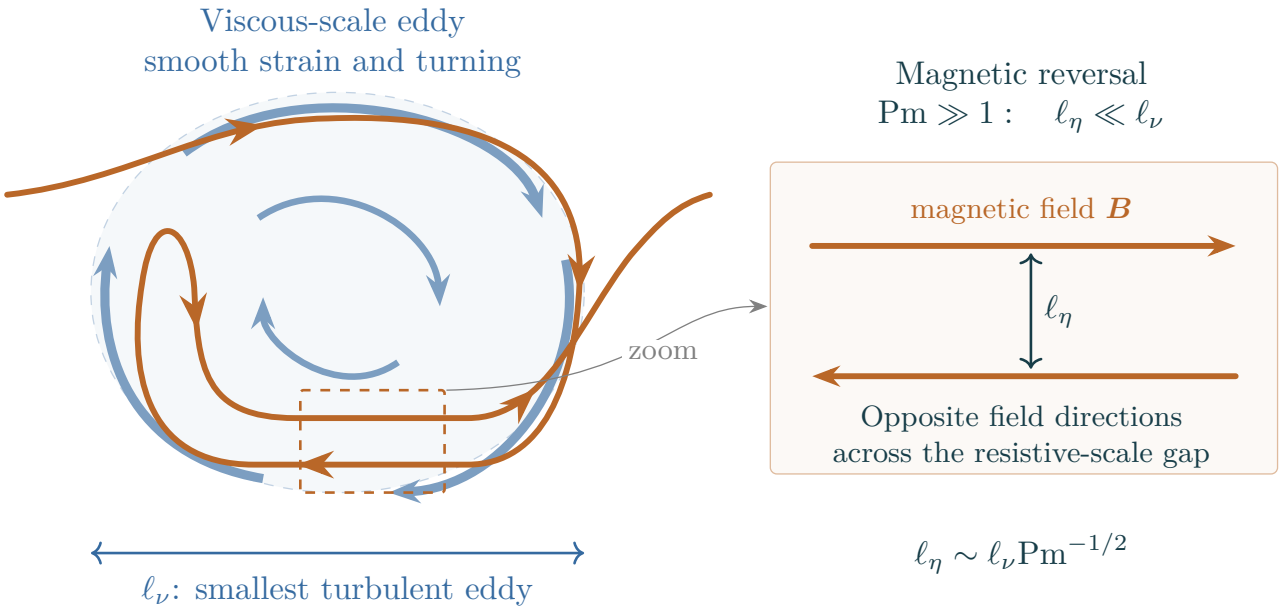


Figure 11: Viscous-scale motion and resistive-scale field reversal at high magnetic Prandtl number. Blue arrows represent the smallest turbulent eddy, of size ℓ_ν; orange curves represent magnetic field. The smooth velocity gradients stretch and turn the field, producing adjacent, oppositely directed segments separated by $\ell_\eta \ll \ell_\nu$. The enlarged gap marks the reversal scale, not the thickness of a drawn line. This is a schematic projection of three-dimensional deformation, with the separation exaggerated for visibility; below ℓ_ν the velocity is smooth, not a new cascade of smaller eddies [20, 33].

6.4 Brief contrast: low magnetic Prandtl number

For $\mathrm{Pm} \ll 1$, the ordering reverses: $\ell_\nu \ll \ell_\eta \ll L$. Magnetic diffusion becomes important while velocity fluctuations are still in the inertial range. The same balance now uses the strain of the eddy at ℓ_η:

$$\frac{\eta}{\ell_\eta^2} \sim \epsilon^{1/3}\ell_\eta^{-2/3} \quad \Longrightarrow \quad \ell_\eta \sim \left(\frac{\eta^3}{\epsilon}\right)^{1/4} \sim L\mathrm{Rm}^{-3/4}. \tag{6.5}$$

If eddies at ℓ_η control growth well above onset, $\gamma_E \sim (U/L)\mathrm{Rm}^{1/2}$. The fastest gradients at ℓ_ν no longer set this estimate. Low-Pm dynamo is possible, but this scaling does not calculate its threshold [21, 29].

Comparing the two scale orderings

Figure 12(a) shows the high-Pm case used in the main discussion; panel (b) illustrates the low-Pm contrast. To read the spectral diagrams, define the one-dimensional spectra by

$$\frac{\rho\langle U^2\rangle}{2} = \int E_K(k)\,\mathrm{d}k, \qquad \frac{\langle B^2\rangle}{8\pi} = \int M(k)\,\mathrm{d}k, \qquad k_\nu \sim \ell_\nu^{-1}, \quad k_\eta \sim \ell_\eta^{-1}. \tag{6.6}$$

Both spectra thus have the same energy-density normalization. Increasing k means decreasing length. On logarithmic axes, the energy in a logarithmic interval is proportional to $kE_K(k)$ or $kM(k)$, rather than the unweighted area on the page.

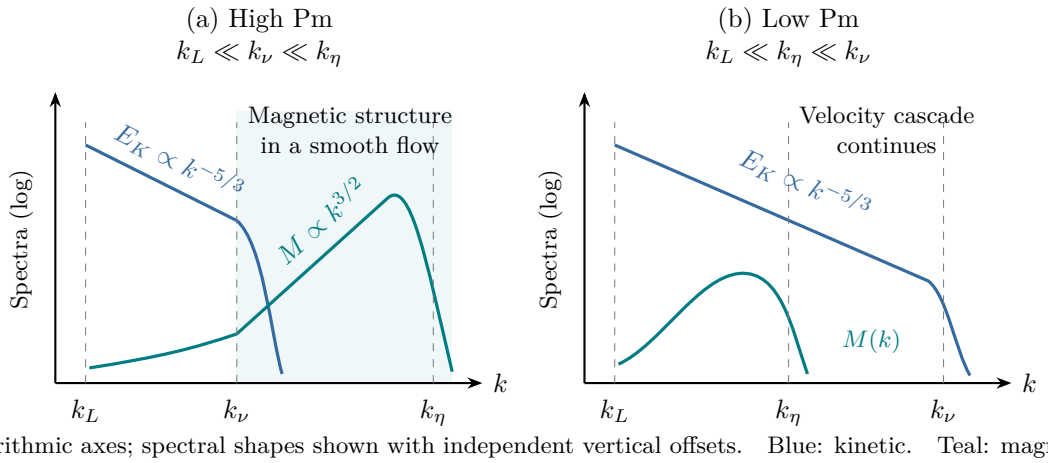


Figure 12: Two kinematic regimes. At high Pm, magnetic structure extends beyond the velocity cutoff; at low Pm, magnetic diffusion intervenes inside the velocity inertial range. The high-Pm magnetic slope is the smooth-flow Kazantsev result discussed below. No universal low-Pm magnetic slope is assigned. Cutoffs are illustrative; the kinetic and magnetic curves are shifted vertically to show their shapes, so their plotted heights should not be used to infer energy ratios. These are schematics of the regimes discussed in [20, 29], with the high-Pm slope from [28].

6.5 High magnetic Prandtl number: the kinematic spectrum

We now return to $\mathrm{Pm} \gg 1$. Kazantsev's original random-flow calculation [28] provides a tractable statistical model: the velocity is prescribed, homogeneous, isotropic, and Gaussian, with zero correlation time. Its smooth-flow, high-Pm limit gives a growing magnetic spectrum with

$$M(k,t) \propto e^{\gamma_E t} k^{3/2}, \qquad k_\nu \ll k \ll k_\eta, \tag{6.7}$$

followed by a resistive cutoff [28, 20]. In this range $kM(k) \propto k^{5/2}$, so the magnetic energy is concentrated toward the resistive end. The full statistical calculation supplies the spectrum; the short stretching–diffusion balance supplies its characteristic cutoff. For a guided derivation of the spectral equation and its growing solution, see Rincon [24, Section 3.4.8].

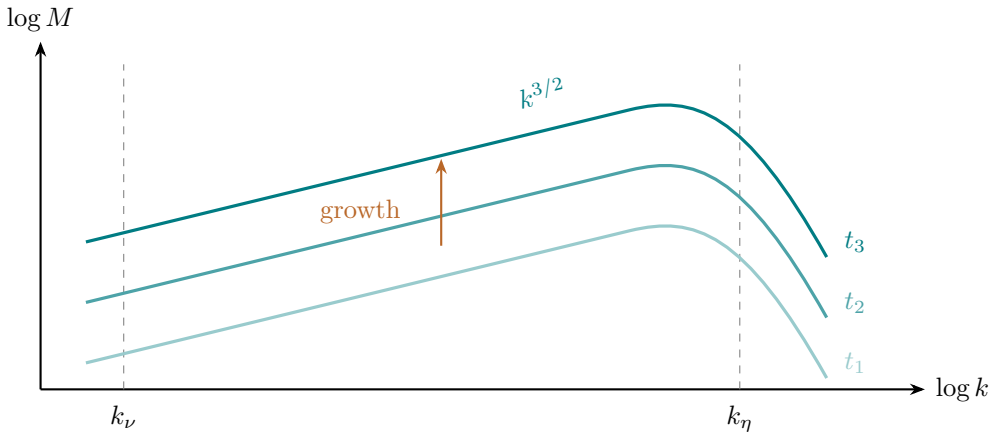


Figure 13: A schematic growing kinematic eigenmode after the initial transient. The flow remains prescribed, so the spectrum rises without needing to move its resistive cutoff. This is not a constant-flux Kolmogorov spectrum and should not be extrapolated into the nonlinear stage. The curves illustrate the smooth-flow Kazantsev solution [28, 20], rather than data from a particular run.

The spectrum and the folded-field picture describe the same organization in different ways: rapid transverse reversals produce power at large k, even though the flow doing the stretching varies on a larger scale. High magnetic energy at large k does not imply that the field consists only of small, tightly curved loops.

7 Back reaction, nonlinear growth, and saturation

7.1 Which motions feel the field first?

Magnetic tension tends to straighten bent field lines. Its force per unit volume and the corresponding acceleration are

$$\boldsymbol{f}_{\rm tens} = \frac{(\boldsymbol{B}\cdot\boldsymbol{\nabla})\boldsymbol{B}}{4\pi}, \qquad \boldsymbol{a}_{\rm tens} = \frac{\boldsymbol{f}_{\rm tens}}{\rho}.$$

In the folded-field estimate, the along-field variation scale is ℓ_s, giving $a_{\rm tens} \sim B^2/(4\pi\rho\ell_s)$. The short transverse reversal scale ℓ_η does not set this tension. Comparing with the eddy's inertial acceleration gives

$$\frac{B^2}{4\pi\rho\ell_s} \sim \frac{\delta U_{\ell_s}^2}{\ell_s} \quad\Longrightarrow\quad \frac{B^2}{4\pi\rho} \sim \delta U_{\ell_s}^2. \tag{7.1}$$

When these accelerations are comparable, tension can change the eddy's velocity substantially within one turnover time, suppressing its ability to stretch the field [20, Section 5.2.1, Eqs. (62) and (64)].

Initially $\ell_s \sim \ell_\nu$. The fastest, smallest stretching eddies are therefore modified first, when the magnetic energy is comparable to their energy. Since $\delta U_{\ell_\nu}^2/U^2 \sim {\rm Re}^{-1/2}$, this can happen far below the total turbulent kinetic energy.

> The end of exponential kinematic growth is not the end of the dynamo. Larger eddies are slower, but contain more energy and can continue stretching a field that already resists the smallest eddies.

7.2 Nonlinear growth and approach to equipartition

A useful nonlinear model lets the dominant stretching scale move to larger eddies as the field strengthens. Define $e_B = \langle B^2\rangle/(8\pi)$. Equation (7.1) gives $e_B/\rho \sim \delta U_{\ell_s}^2$ to order unity, and hence the short estimate

$$\frac{1}{\rho}\frac{{\rm d}e_B}{{\rm d}t} \sim \frac{\delta U_{\ell_s}}{\ell_s}\frac{e_B}{\rho} \sim \frac{\delta U_{\ell_s}^3}{\ell_s} \sim \epsilon. \tag{7.2}$$

The first estimate is magnetic energy times the stretching rate; the last uses the Kolmogorov flux $\delta U_{\ell_s}^3/\ell_s \sim \epsilon$ [20, Section 5.2.1, Eq. (63)].

Allowing for the fraction of turbulent power that becomes net magnetic growth,

$$\frac{{\rm d}e_B}{{\rm d}t} \sim C_E\rho\epsilon. \tag{7.3}$$

Continued forcing can therefore produce an approximately linear magnetic-energy growth stage. This is a phenomenological description of an intermediate regime with adequate scale separation; it is not an exact growth law for every dynamo [20, 23].

In the folded-field model, the longer stretching time also gives diffusion more time to act: $\ell_\eta \sim (\eta\tau_s)^{1/2}$, where $\tau_s \sim \ell_s/\delta U_{\ell_s}$ is the turnover time at the stretching scale. As ℓ_s grows, τ_s increases and the effective reversal scale can grow. This motivates the evolving spectral shapes in Figure 14; it does not fix a unique saturated spectral index.

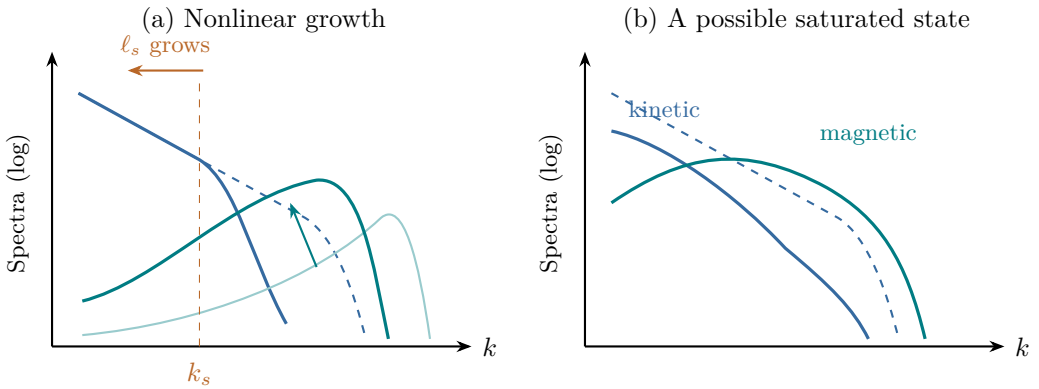


Figure 14: Qualitative spectral evolution in a high-Pm folded-field model. (a) Back reaction modifies the small-scale strain; larger eddies remain available, and magnetic energy spreads to larger scales. The marker $k_s \sim \ell_s^{-1}$ identifies the evolving stretching scale, not necessarily a crossing of the spectra. (b) One illustrative broad saturated spectrum. Its slopes, peak, cutoffs, and kinetic-to-magnetic ratio are not universal; a spectral shape alone does not establish saturation [20, 22].

When the growing field also modifies the energy-containing eddies, a useful estimate of its saturated strength is approximate equipartition:

$$\frac{\langle B^2 \rangle}{8\pi} \sim \frac{\rho \langle U^2 \rangle}{2}. \tag{7.4}$$

This is an order-of-magnitude estimate, not an exact equality or a requirement that kinetic and magnetic spectra coincide at every wavenumber [20, 24].

Figure 15 collects the stages: exponential kinematic growth, a slower nonlinear growth phase, and fluctuations around a saturated mean.

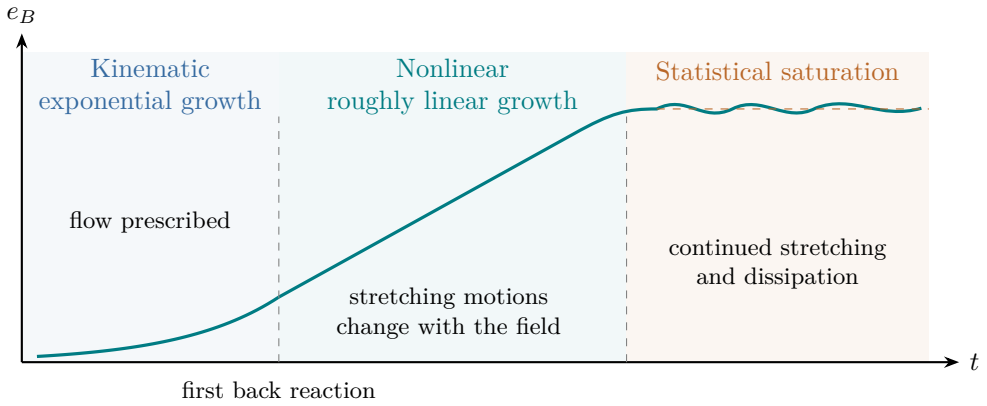


Figure 15: A schematic magnetic-energy history under continued forcing, with linear axes. The time intervals and amplitudes are illustrative. The intermediate linear-growth stage need not be clearly separated when the range of turbulent scales is short. The sequence summarizes the nonlinear-growth picture discussed in [20, 23]; the curve is illustrative.

7.3 Connections to reconnection and plasma physics

Stretching and folding build sharp magnetic gradients. Diffusion and reconnection can dissipate magnetic structure and change its connectivity as the dynamo continually reorganizes it. To determine their dynamical role, compare the rates of structure formation and disruption and check the energy budget;

their presence alone does not specify a saturation law. Schekochihin [30, Sections 13.2–13.3] reviews numerical evidence and proposed reconnection-limited dynamo models.

In weakly collisional plasma, a field that starts to magnetize particles also changes the stress response. Stretching generates pressure anisotropy, and kinetic instabilities can modify scattering and the motions doing the stretching. A prescribed scalar viscosity may then be insufficient. Simulations connecting Weibel seeds to turbulent amplification illustrate the link from large-scale forcing to microscopic magnetization and back to macroscopic magnetic dynamics [17]. The CGL and kinetic-turbulence topics will develop this connection.

Follow three things together: the energy source, the scale doing the stretching, and the geometry of the resulting field. Kinematic growth uses a nearly prescribed flow; nonlinear growth changes that flow; saturation brings the field to a dynamically significant strength.

Recommended reading

Start with a review: Dynamo theories. François Rincon's *Dynamo theories* [24] is the recommended starting point. Read Section 2 for the induction equation, dimensionless numbers, and anti-dynamo theorems, then Section 3 for small-scale dynamos. Sections 3.2–3.3 give the physical picture and the two Pm regimes; Sections 3.4 and 3.5 cover kinematic theory and nonlinear evolution. The more technical calculations can be left for a second reading.

Observational context and possible origins. Start with the introduction and observational discussion in Durrer & Neronov [1]. Read it for the field-strength–correlation-length map and the distinction between primordial and astrophysical scenarios. Vazza et al. [2] connect these questions to cosmic-web radio observations; Vovk et al. [5] give a compact example of the pair-echo argument.

Biermann battery and Weibel. Biermann's original paper [25] is the classic starting point for the battery mechanism. The two short original papers by Weibel [10] and Fried [11] introduce the anisotropy-driven instability and its physical interpretation. Huntington et al. [12] provide a laboratory example of magnetic-field generation in counter-streaming plasma flows. For a classic numerical example, Silva et al. [26] use three-dimensional, fully kinetic PIC simulations of interpenetrating electron–positron plasma shells to follow filamentation and magnetic-field generation. Schoeffler et al. [6] provide an example of the interplay between Biermann fields and Weibel instability. Read these examples with attention to the source of free energy, the species carrying the unstable current, and the scale of the generated field.

Dynamo foundations and turbulent amplification. Moffatt [18] provides the classical kinematic framework and anti-dynamo theorems. Schekochihin et al. [20] connect high-Pm scales, folded fields, and spectra to simulations; read the growth curves and field geometry first. Beresnyak [23] discusses the nonlinear conversion of turbulent power into magnetic growth. In Schekochihin's *MHD turbulence: a biased review* [30], Section 13.1 revisits folded fields and the classical saturation arguments, Section 13.2 presents numerical evidence for reconnection, and Section 13.3.2 gives the nonlinear-growth scaling. Sections 13.3–13.4 offer further discussion of reconnection and proposed saturation scenarios.

References

[1] R. Durrer and A. Neronov, "Cosmological magnetic fields: their generation, evolution and observation," *Astronomy and Astrophysics Review* **21**, 62 (2013). 10.1007/s00159-013-0062-7.

[2] F. Vazza et al., "Magnetogenesis and the Cosmic Web: A Joint Challenge for Radio Observations and Numerical Simulations," *Galaxies* **9**, 109 (2021). 10.3390/galaxies9040109.

[3] Hitomi Collaboration, "The quiescent intracluster medium in the core of the Perseus cluster," *Nature* **535**, 117–121 (2016). 10.1038/nature18627.

[4] A. Neronov and I. Vovk, "Evidence for Strong Extragalactic Magnetic Fields from Fermi Observations of TeV Blazars," *Science* **328**, 73–75 (2010). 10.1126/science.1184192.

[5] I. Vovk, A. Korochkin, A. Neronov, and D. Semikoz, "Constraints on the intergalactic magnetic field from Fermi/LAT observations of the 'pair echo' of GRB 221009A," *Astronomy & Astrophysics* **683**, A25 (2024). 10.1051/0004-6361/202347310.

[6] K. M. Schoeffler et al., "The generation of magnetic fields by the Biermann battery and the interplay with the Weibel instability," *Physics of Plasmas* **23**, 056304 (2016). 10.1063/1.4946017.

[7] K. M. Schoeffler and L. O. Silva, "Effects of collisions on the generation and suppression of temperature anisotropies and the Weibel instability," *Physical Review Research* **2**, 033233 (2020). 10.1103/PhysRevResearch.2.033233.

[8] L. Willingale et al., "Fast Advection of Magnetic Fields by Hot Electrons," *Physical Review Letters* **105**, 095001 (2010). 10.1103/PhysRevLett.105.095001.

[9] L. Willingale et al., "Proton deflectometry of a magnetic reconnection geometry," *Physics of Plasmas* **17**, 043104 (2010). 10.1063/1.3377787.

[10] E. S. Weibel, "Spontaneously Growing Transverse Waves in a Plasma Due to an Anisotropic Velocity Distribution," *Physical Review Letters* **2**, 83–84 (1959). 10.1103/PhysRevLett.2.83.

[11] B. D. Fried, "Mechanism for Instability of Transverse Plasma Waves," *Physics of Fluids* **2**, 337 (1959). 10.1063/1.1705933.

[12] C. M. Huntington et al., "Observation of magnetic field generation via the Weibel instability in interpenetrating plasma flows," *Nature Physics* **11**, 173–176 (2015). 10.1038/nphys3178.

[13] C. Zhang et al., "Mapping the self-generated magnetic fields due to thermal Weibel instability," *Proceedings of the National Academy of Sciences* **119**, e2211713119 (2022). 10.1073/pnas.2211713119.

[14] K. V. Lezhnin et al., "Simulations of self-magnetization in expanding high-energy-density plasmas" (2025), arXiv:2503.15624v1; revised as "Expansion-Driven Self-Magnetization of High-Energy-Density Plasmas" (2026), arXiv:2503.15624.

[15] M. V. Medvedev and A. Loeb, "Generation of Magnetic Fields in the Relativistic Shock of Gamma-Ray Burst Sources," *Astrophysical Journal* **526**, 697–706 (1999). 10.1086/308038.

[16] M. Zhou et al., "Spontaneous magnetization of collisionless plasma," *Proceedings of the National Academy of Sciences* **119**, e2119831119 (2022). 10.1073/pnas.2119831119.

[17] M. Zhou et al., "Magnetogenesis in a Collisionless Plasma: From Weibel Instability to Turbulent Dynamo," *Astrophysical Journal* **960**, 12 (2024). 10.3847/1538-4357/ad0b0f.

[18] H. K. Moffatt, *Magnetic Field Generation in Electrically Conducting Fluids*, Cambridge University Press (1978).

[19] T. G. Cowling, "The Magnetic Field of Sunspots," *Monthly Notices of the Royal Astronomical Society* **94**, 39–48 (1933). 10.1093/mnras/94.1.39.

[20] A. A. Schekochihin et al., "Simulations of the Small-Scale Turbulent Dynamo," *Astrophysical Journal* **612**, 276–307 (2004). 10.1086/422547.

[21] A. A. Schekochihin et al., "The Onset of a Small-Scale Turbulent Dynamo at Low Magnetic Prandtl Numbers," *Astrophysical Journal* **625**, L115–L118 (2005). arXiv:astro-ph/0412594.

[22] A. A. Schekochihin et al., "Saturated State of the Nonlinear Small-Scale Dynamo," *Physical Review Letters* **92**, 084504 (2004). 10.1103/PhysRevLett.92.084504.

[23] A. Beresnyak, "Universal Nonlinear Small-Scale Dynamo," *Physical Review Letters* **108**, 035002 (2012). 10.1103/PhysRevLett.108.035002.

[24] F. Rincon, "Dynamo theories," *Journal of Plasma Physics* **85**, 205850401 (2019). 10.1017/S0022377819000539.

[25] L. Biermann, "Über den Ursprung der Magnetfelder auf Sternen und im interstellaren Raum," *Zeitschrift für Naturforschung A* **5**, 65–71 (1950). 10.1515/zna-1950-0201.

[26] L. O. Silva, R. A. Fonseca, J. W. Tonge, J. M. Dawson, W. B. Mori, and M. V. Medvedev, "Interpenetrating Plasma Shells: Near-Equipartition Magnetic Field Generation and Nonthermal Particle Acceleration," *Astrophysical Journal Letters* **596**, L121–L124 (2003). 10.1086/379156.

[27] G. K. Batchelor, "On the spontaneous magnetic field in a conducting liquid in turbulent motion," *Proceedings of the Royal Society A* **201**, 405–416 (1950). 10.1098/rspa.1950.0069.

[28] A. P. Kazantsev, "Enhancement of a Magnetic Field by a Conducting Fluid," *Soviet Physics JETP* **26**, 1031–1034 (1968); Russian original published in 1967. Full text.

[29] A. A. Schekochihin et al., "Fluctuation dynamo and turbulent induction at low magnetic Prandtl numbers," *New Journal of Physics* **9**, 300 (2007). 10.1088/1367-2630/9/8/300.

[30] A. A. Schekochihin, "MHD turbulence: a biased review," *Journal of Plasma Physics* **88**, 155880501 (2022). 10.1017/S0022377822000721.

[31] S. I. Vainshtein and Ya. B. Zel'dovich, "Origin of Magnetic Fields in Astrophysics (Turbulent 'Dynamo' Mechanisms)," *Soviet Physics Uspekhi* **15**, 159–172 (1972). 10.1070/PU1972v015n02ABEH004960.

[32] A. Shukurov, D. Sokoloff, and A. Schekochihin, "Special issue: Macroscopic randomness in astrophysical plasmas: The legacy and vision of Ya. B. Zeldovich," *Journal of Plasma Physics* **81**, 391810403 (2015). 10.1017/S0022377815000355.

[33] M. W. Kunz, T. W. Jones, and I. Zhuravleva, "Plasma Physics of the Intracluster Medium," in *Handbook of X-ray and Gamma-ray Astrophysics*, pp. 5049–5090 (2024). 10.1007/978-981-19-6960-7_125. arXiv:2205.02489.